Observations and Numerical Simulation of the Effects of the 21 August 2017 North American Total Solar Eclipse on Surface Conditions and Atmospheric Boundary-Layer Evolution

Michael S. Buban, Temple R. Lee, Edward J. Dumas, C. Bruce Baker & Mark Heuer

Springer

Springer

RESEARCH ARTICLE

CrossMark

Observations and Numerical Simulation of the Effects of the 21 August 2017 North American Total Solar Eclipse on Surface Conditions and Atmospheric Boundary-Layer Evolution
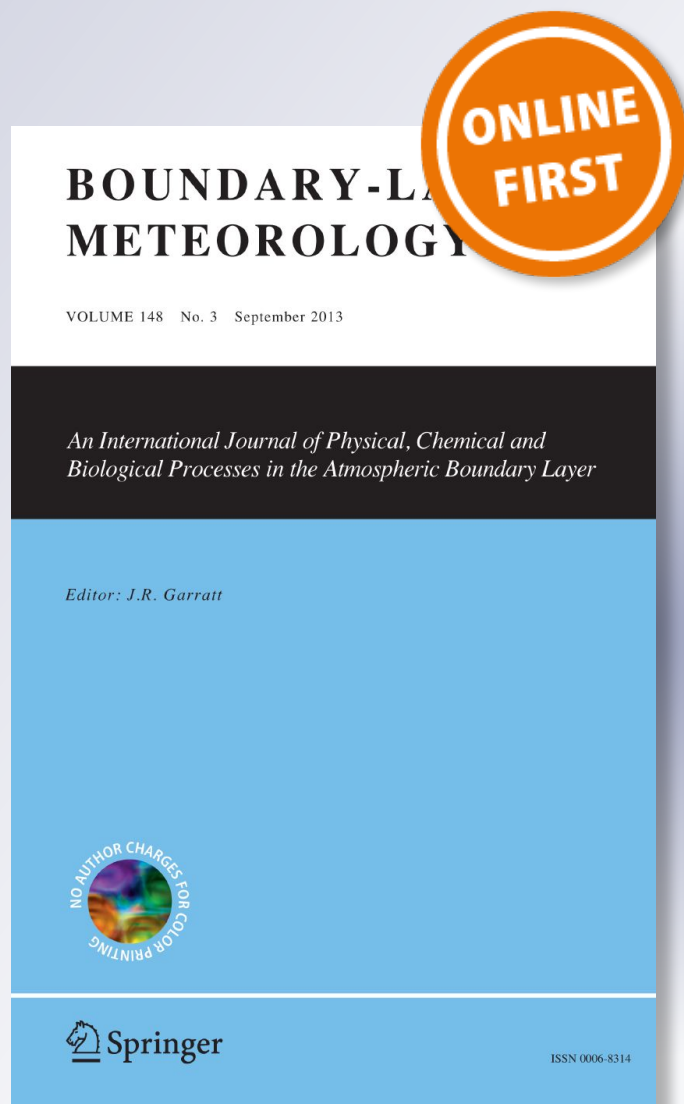
Michael S. Buban[1,2] · **Temple R. Lee[1,2]** · **Edward J. Dumas[3]** · **C. Bruce Baker[2]** · **Mark Heuer[3]**

Abstract

We present unique observations of a total solar eclipse from a small unmanned aircraft system (sUAS) platform that was operated during the 21 August 2017 North American solar eclipse. The observations were collected near Ten Mile, Tennessee, where eclipse totality lasted 2 min 38 s. A 2-m micrometeorological tripod was erected on-site to measure surface and air temperature, near-surface water vapour, incoming and outgoing shortwave and longwave radiative fluxes, and turbulent fluxes. The sUAS platform and micrometeorological tripod observations indicate significant cooling below a height of 50 m above ground level (a.g.l.) during and shortly after totality. Near-surface temperatures do not return to pre-eclipse values until about 60 min following totality. Above about 50 m a.g.l., smaller temperature changes are observed during the eclipse, as the duration of the eclipse has less influence on deeper boundary-layer turbulence. Additionally, the sensible heat flux becomes slightly negative around totality, and the turbulence kinetic energy and vertical velocity variance concurrently decrease. The evolution of the near-surface meteorological fields are investigated in more detail using a large-eddy simulation (LES) model. The simulations generally reproduce the observations well, in terms of the timing and magnitude of changes in temperature, moisture and sensible and latent heat fluxes. However, the LES model slightly underestimates the diurnal range and decrease in temperature during the eclipse while overestimating the sensible heat fluxes.

Keywords Eclipse · Large-eddy simulation · Sensible heat flux · Small unmanned aircraft systems

✉ Michael S. Buban
  Michael.buban@noaa.gov

1 Cooperative Institute for Mesoscale Meteorological Studies (CIMMS), Oak Ridge, TN 37830, USA

2 NOAA/OAR/ARL Atmospheric Turbulence and Diffusion Division, Oak Ridge, TN 37830, USA

3 Oak Ridge Associated Universities, Oak Ridge, TN 37830, USA

🙎 Springer

1 Introduction

Although total solar eclipses occur several times a year around the globe, they are a relatively rare phenomenon at any given point on the Earth's surface. At totality, only diffuse shortwave radiation is incident upon the Earth's surface, and conditions on Earth resemble those just after (prior to) sunset (sunrise). This decrease in incoming shortwave radiation can have a marked effect on the surface radiation balance and the structure of the lower atmospheric boundary layer (ABL). Previous studies have examined the effect of both partial and total solar eclipses on near-surface conditions, with many studies showing surface temperature decreases from 2 to 5 °C (e.g., Anderson et al. 1972; Segal et al. 1996; Foken et al. 2001; Founda et al. 2007; Mauder et al. 2007; Lee et al. 2018) up to as much as 10 °C (Stewert and Rouse 1974). Decreases in both the sensible heat flux (H) and latent heat flux (LE) have also been noted. For example, Eaton et al. (1997) and Mauder et al. (2007) found both sensible and latent heat flux values decreasing to zero during the minimum in solar radiation. Decreases in near-surface wind speeds have also been observed during totality (e.g., Anderson and Keefer 1975; Subrahamanyam et al. 2011; Turner et al. 2018).

On 21 August 2017, several meteorological instruments were deployed near Ten Mile, Tennessee, USA, to observe a total solar eclipse; the entire eclipse lasted for 2 h 55 min, with the total eclipse lasting for 2 min 38 s. Unlike previous studies that used conventional meteorological instrumentation, the present study combines measurements from a micrometeorological tripod with measurements from a small unmanned aircraft system (sUAS) platform so as to investigate the temporal evolution of surface and near-surface atmospheric conditions. To further interpret the results, a large-eddy simulation (LES) model was used, and results compared to observations.

2 Measurements

The study site was located near Ten Mile, Tennessee, approximately 75 km south-west of Knoxville (Fig. 1). At the site, a 2-m tripod was installed with an aspirated platinum resistance thermometer, infrared thermometer for measuring land-surface temperature, a net radiometer to measure incoming and outgoing radiation components, a sonic anemometer to determine heat and turbulent fluxes, and an infrared gas analyzer to measure water vapour concentration from which latent heat fluxes could be derived.

In addition to these surface and near-surface atmospheric measurements, a DJI S-1000 sUAS platform (DJI, Shenzhen, Guangdong, China) was operated; details on the DJI S-1000 sUAS platform are discussed in Dumas et al. (2016) and Lee et al. (2017, 2019). Two iMet-XQ sensors (International Met Systems Inc., Kentwood, Michigan, USA), were mounted on top of the sUAS platform to measure temperature and pressure at 1 Hz. The iMet-XQ sensors have a manufacturer-stated accuracy of ± 0.3 °C and ± 1.5 hPa for temperature and pressure, respectively (e.g., Lee et al. 2017). The sUAS platform flew up to a height of 365 m above ground level (a.g.l.) to characterize the ABL temperature evolution. On the underside of the sUAS platform was a downward-pointing FLIR Tau 2 infrared camera (FLIR Systems Inc., Wilsonville, Oregon, USA) comprising a 7.5-mm lens with a 45° view angle and 336×256 pixel resolution and able to measure surface temperature at 1 Hz (Dumas et al. 2016).

A total of eight flights were flown on 21 August; four flights were made prior to totality (at 150 min, 90 min, 60 min, and 30 min prior to totality), and three flown after totality (at 30 min, 60 min, and 90 min after totality) with an average flight time of approximately
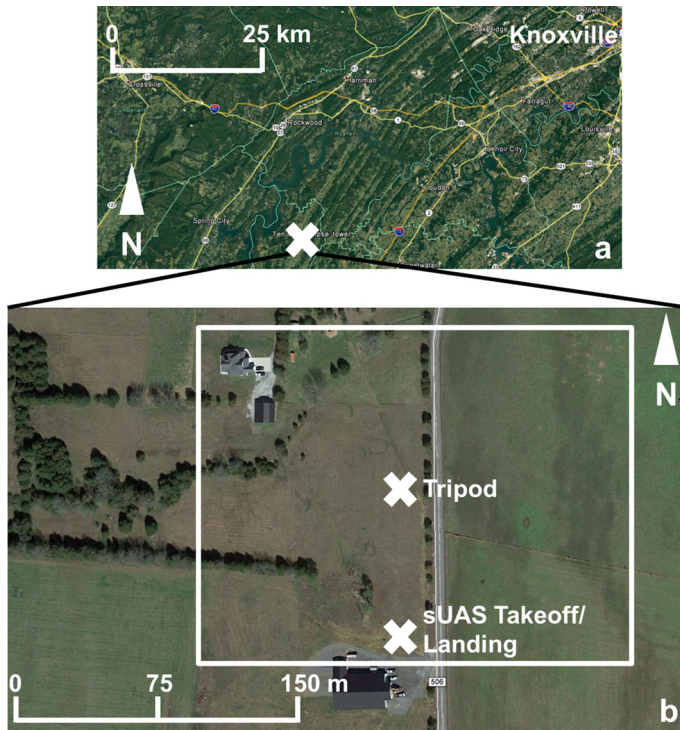
Fig. 1 Location of the study site relative to Knoxville, Tennessee (**a**). **b** A zoomed in map of study site, with the locations of the sUAS takeoff and landing noted relative to the instrumented 2-m tripod. White box in **b** the approximate area shown in Figs. 7 and 8. Images are courtesy of GoogleEarth

12.5 min. An additional flight was flown about 5 min prior to totality. During all of these flights, the sUAS platform hovered at 365 m a.g.l. above the tripod for 2–4 min to sample changes in air temperature and land-surface temperature.

3 Numerical Model

The large-eddy simulation (LES) model was based on the Collaborative Model for Multiscale Atmospheric Simulation or COMMAS (e.g., Wicker and Wilhelmson 1995; Coniglio et al. 2006; Buban et al. 2012) with simulations compared with observations collected during the eclipse. The COMMAS model is a cloud-resolving and non-hydrostatic model that includes a weakly-diffusive fifth-order horizontal advection scheme (Wicker and Skamarock 2002), a third-order vertical advection scheme, a 1.5-order parametrization for turbulent kinetic energy (TKE), and a modified force-restore land-surface–atmosphere exchange scheme (Deardorff 1978; Peckham et al. 2004; Buban et al. 2012). Within this scheme the surface was treated as horizontally homogeneous, and the simulations used a horizontal grid spacing of 100 m. To capture the rapid low-level evolution of the ABL during the total eclipse, the lowest 25 grid levels had a vertical spacing of 6 m, with the lowest model level at 3 m a.g.l. Above 150 m, the grid was stretched, culminating in a grid spacing of 50 m at the top of the domain. The domain size was 36 km × 36 km × 6 km for the x, y, and z dimensions, respectively,
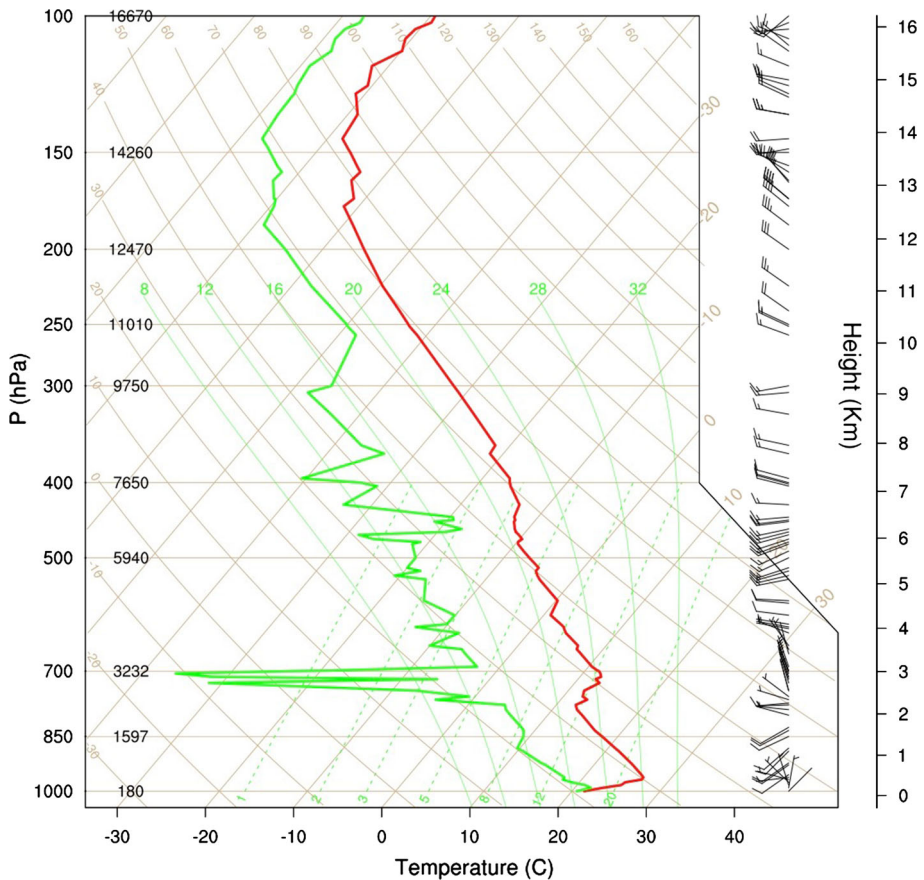
Fig. 2 Skew-T diagram of temperature (red line), and dewpoint temperature (green line) at 0800 local daylight time (1200 UTC) 21 August 2017 at Nashville, Tennessee

and periodic lateral boundary conditions were applied. The model was initialized using the 0800 LDT (local daylight time = UTC − 4 h) sounding from Nashville, Tennessee, which is located approximately 200 km west of the Ten Mile site (Fig. 2). Nashville was the nearest sounding site, and conditions were synoptically homogeneous over the entire region. The simulation was run for 12 h covering the daylight period following the sounding launch.

4 Results

4.1 Pre-eclipse Conditions

Early morning conditions were fairly quiescent over the mid-south USA, as represented by the Nashville sounding (Fig. 2). A low-level inversion had set up with saturated conditions near the surface and dew covering the ground, with patches of fog scattered throughout the area. Above the surface, drier air was found with low wind speeds throughout the depth of the troposphere. Throughout the morning and into the afternoon, surface and 1.5-m temperatures gradually increased by about 10 °C, and 1.5-m dewpoints decreased by about 4 °C as the
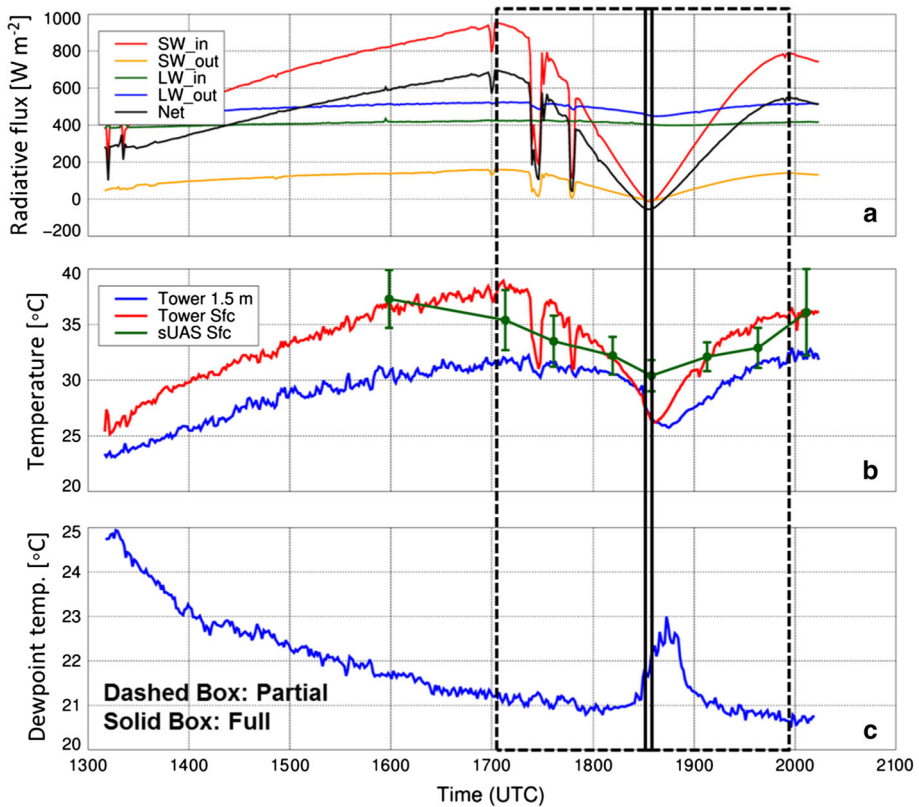
Fig. 3 Radiative flux components during daytime on 21 August 2017 (**a**). Red, orange, green, blue, and black lines show incoming shortwave radiative flux, outgoing shortwave radiative flux, incoming longwave radiative flux, outgoing longwave radiative flux, and net radiative flux, respectively. **b** Surface temperature (red line), air temperature measured 1.5 m a.g.l. (blue line), and surface temperature (filled circle) and standard deviation (vertical bars) measured from the sUAS platform (green) whereas **c** dewpoint temperature. 1-min means are used in all analyses. The dashed black box denotes the eclipse period with the solid vertical lines depicting the period of totality

vertical mixing and ABL growth commenced (Fig. 3). Similar low-level ABL warming and drying is also seen in the LES model results (Fig. 4), however the magnitudes of these changes are slightly lower. One consideration is that the lowest model level is at 3 m a.g.l. and therefore would be expected to have smaller changes than at the 1.5-m observation level. Additionally, the simulation had a cool bias in the temperatures and a dry bias in the dewpoints. By early afternoon, the lower atmosphere developed ABL-topped cumuli as lifted condensation levels were achieved, as indicated by the sharp decreases in incoming shortwave radiation (Fig. 3a). ABL-topped cumuli also developed in the LES model by early afternoon (Fig. 5a).

4.2 Conditions During the Eclipse

The partial eclipse began at 1303:37 local daylight time, with totality lasting from 1432:07 through 1434:46 local daylight time, and ended at 1558:13 local daylight time over the study site. As the partial eclipse began, the incoming shortwave radiative flux decreased
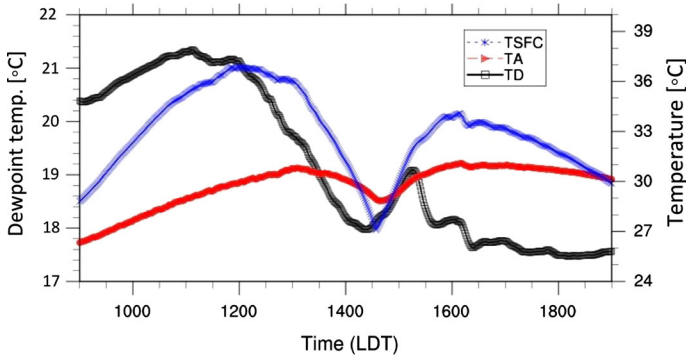
Fig. 4 Surface temperature (blue line), 3 m air temperature (red line), and 3 m dewpoint (black line) from the simulation
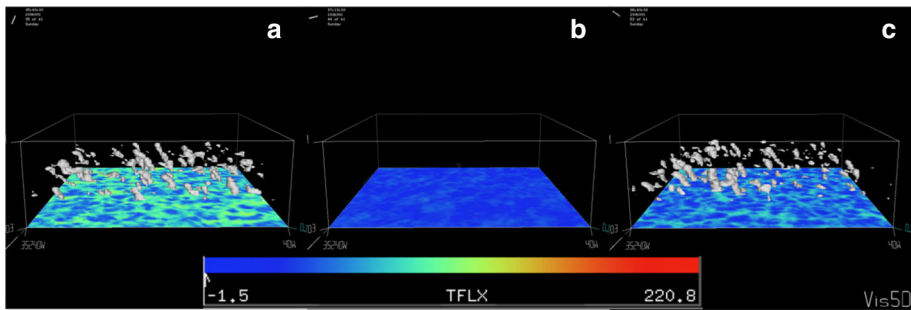

Fig. 5 Surface sensible heat flux (colour filled) and cloud water content > 0.05 g kg^{-1} (white surfaces) at 1340 (**a**), 1510 (**b**) and 1640 (**c**) LDT

from ≈ 900 W m^{-2} to zero during totality (Fig. 3a). After totality, the shortwave radiative flux steadily increased to ≈ 800 W m^{-2}. The outgoing shortwave radiative flux showed an immediate response, decreasing to zero during totality. Note the sharp localized decreases in incoming and outgoing shortwave and net radiative fluxes as clouds passed over the site.

The outgoing longwave radiative flux showed a decrease during the eclipse period, with a smaller decrease ≈ 100 W m^{-2} during the event. The incoming longwave radiative flux showed a very slight decrease; however, the longwave radiative flux components showed a time lag, with minimum values just after totality ended. The temperatures showed a decrease during the eclipse with the surface temperature decreasing by ≈ 12 °C and 1.5-m temperatures decreasing by ≈ 5 °C (Fig. 3b). There was a time lag in the temperature changes as minimum values occurred just after totality ended with a greater lag in the 1.5-m temperature (≈ 13 min) compared to the surface temperature (≈ 4 min). Both temperatures then steadily increased as the eclipse continued.

Results from the simulation parallel those of the observations with surface temperatures decreasing ≈ 9 °C and 3-m temperatures decreasing by ≈ 1.5 °C (Fig. 4). The decrease in temperatures is consistent with the bias of a smaller diurnal increase in temperatures in the model prior to the eclipse. The simulated temperatures also show a time lag in the minima, with the 3-m temperature lag greater (≈ 5 min) than the surface temperature lag (≈ 1 min). These time lags are smaller than those observed.
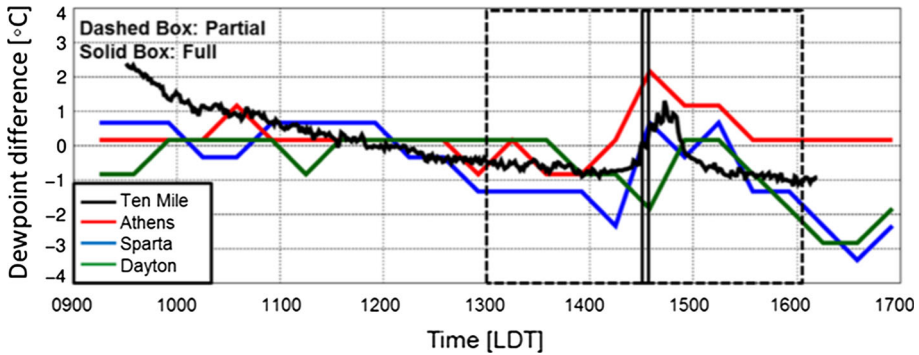
Fig. 6 Time series of dewpoint temperature with the mean value between 1100 and 1300 LDT subtracted at three sites in eastern Tennessee compared with observations from Ten Mile. Athens is approximately 25 km south-east of Ten Mile; Sparta is about 80 km north-west of Ten Mile; and Dayton is 35 km to the south-west

The observed dewpoint temperature showed an interesting steady decrease at a rate similar to that before the eclipse began until just prior to the start of totality when it spiked higher by ≈ 2 °C, peaking after totality ended, then decreasing rapidly until the middle part of the partial phase before steadily decreasing thereafter (Fig. 3c). This feature was also found in the LES model, where approximately a 3 °C dewpoint increase developed, with the increase lasting longer in the simulations than the observations. These moisture profiles were also seen at three other nearby sites that were in the path of totality (Fig. 6). Each of these sites experienced an increase in dewpoint temperature by ≈ 2–3 °C for about 30 min before decreasing to below pre-eclipse values.

Changes in land-surface temperature were further examined using measurements from the FLIR infrared camera mounted on the sUAS platform. From the start of the eclipse until totality, a decrease of about 9 °C was observed (Fig. 7a, b), with a subsequent rise of about 7 °C from just after the end of totality until the end of the eclipse (Fig. 7b, c). This result is more consistent with the model values than the point observations as model results were horizontally averaged. From 1 min prior to totality to 40 s before the end of totality land-surface temperature decreased by about 1 °C (Fig. 8a, b), then by approximately 80 s after totality, the land-surface temperature over the area had increased by about 1.5 °C (Fig. 8b, c) as sunlight returned. Note that the surface temperatures in Fig. 8c are lower than in Fig. 8a, indicative of the temperature lag as seen in the tripod observations.

The sensible heat flux also showed a decrease during the eclipse, decreasing from ≈ 100 W m^{-2} to about -5 W m^{-2} just prior to totality before increasing towards the end of the partial phase of the eclipse as measured at the tripod (Fig. 9a). The latent heat flux showed a larger decrease from ≈ 300 W m^{-2} to about -25 W m^{-2} with a slight lag compared to the sensible heat flux. The sensible and latent heat fluxes in the LES model compare well with the observations in terms of magnitudes and timing of the flux decreases, however there is a large bias in the latent heat flux (Fig. 10). The spatial structure in the sensible heat flux was also computed using tripod data in conjunction with the sUAS platform land-surface temperature (Figs. 7, 8d–f) as in Lee et al. (2017) during the periods that the sUAS platform hovered at 365 m a.g.l. The computed sensible heat fluxes decreased by $\approx 100 - 150$ W m^2 to near zero during totality, before increasing by about 100 W m^2 at the end of the eclipse. Similar patterns were seen in the modelled TKE ($\bar{e}$) and vertical velocity variances (Fig. 9b); however these two variables reached a minimum during the period of totality.
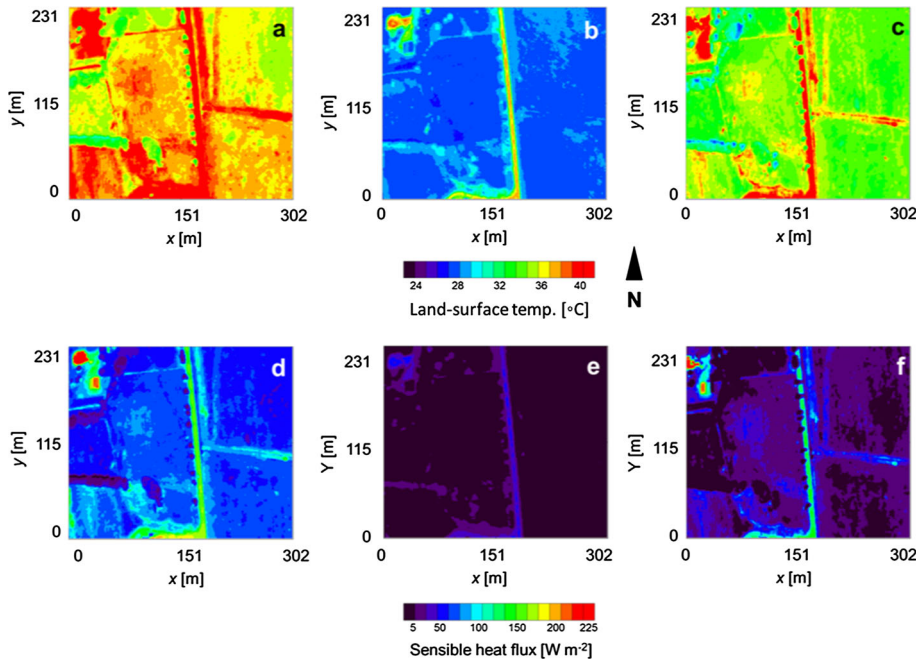
Fig. 7 Land-surface temperatures measured with the FLIR infrared camera onboard the sUAS platform at 1308:41 LDT (**a**), 1432:28 LDT (**b**), and 1606:23 LDT (**c**). Surface sensible heat flux computed from the sUAS platform are shown in **d**–**f** and correspond with the times shown in **a**–**c**

The profiles of temperature between the surface and 365 m a.g.l. obtained from the sUAS platform prior to the eclipse showed the development of a superadiabatic near-surface layer (Fig. 11a), and by 30 min prior to the start of totality, the superadiabatic near-surface layer became neutrally stratified. The flight that began 2 min prior to the start of totality and the flight 30 min after totality ended exhibited a near-surface inversion, with inversion strength peaking at ≈ 1.5–2 °C, with a vertical extent of about 50 m. The flights 60 min and 90 min following totality, however, showed the redevelopment of a neutral near-surface layer towards the end of the partial eclipse (Fig. 11a). Farther aloft, we observed a neutral layer that slowly warmed before and during the first part of the eclipse, cooled slightly near the period of totality, and then warmed again as the eclipse ended (Fig. 11a). During the period leading up to totality the vertical profiles from the LES model are consistent with the sUAS platform observations, showing the development of a superadiabatic layer, then a neutral layer, followed by a ≈ 50-m deep inversion (Fig. 12a). However, the strength of the inversion in the simulation was about half that observed by the sUAS platform. Also, in the sUAS platform observations, a near-neutral layer developed and persisted, whereas the LES showed redevelopment of the near-surface superadiabatic layer. The development of the superadiabatic layer in the LES model but not in the observations may have been due to the treatment of the lower boundary condition. In the LES model, the lower boundary was treated as homogeneous, whereas near the observation site, there was significant heterogeneity, both in land-surface conditions and terrain.

Measurements of water vapour mixing ratio showed a very gradual drying of the ABL aloft throughout the event; however, near the surface there was a slight increase in moisture
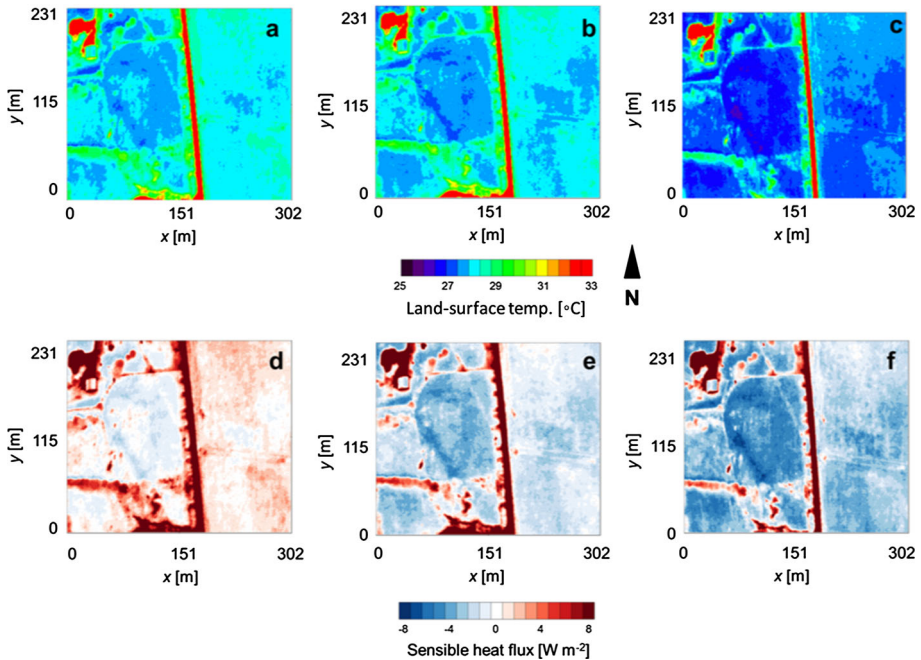
Fig. 8 Land-surface temperatures measured with the FLIR infrared camera onboard the DJI S-1000 (**a–c**) and corresponding surface sensible heat flux (**d–f**) at 1431:06 LDT (left), 1434:06 LDT (middle) and 1436:06 LDT (right)

just after totality ended, before drying continues (Fig. 11b). The observations are consistent with the tripod observations and observations from nearby sites. Similar results are seen in the simulation with drying occurring up to near the start of totality, then an increase in low-level moisture, before drying commences (Fig. 12b). It should be noted that, in addition to the aforementioned dry bias in the model, the model also produces strong moisture lapse rates just above the surface, which were not measured by the sUAS platform. Since the model used homogenous boundary conditions it is possible that local effects in the field of the observations may have contributed to the dry model bias.

5 Discussion and Conclusions

We have described the first known observations of air temperature from a sUAS platform during a total solar eclipse observed on 21 August 2017. These observations allowed us to characterize the evolution of temperature fields between the surface and 365 m a.g.l. We complemented the sUAS platform measurements with surface meteorological and flux observations from a 2-m micrometeorological tripod that was installed near Ten Mile, Tennessee, USA. This site was particularly advantageous because of the long duration (i.e., 2 min 38 s) of eclipse totality and because of the mostly clear, fair-weather conditions that were observed on this day. Also, since the eclipse occurred near the time of peak local heating, this event afforded a unique opportunity to observe the surface and ABL evolution due to rapid changes in shortwave radiation. To complement the observations, a LES model was used, and results
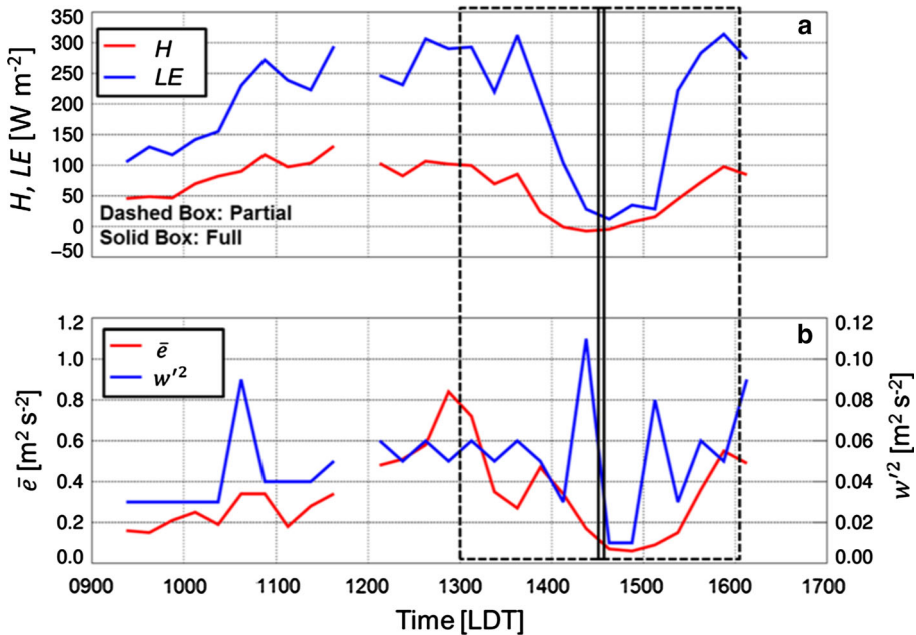
Fig. 9 Sensible ("*H*", red line) and latent ("*LE*", blue line) heat fluxes (**a**). **b** Shows $\bar{e}$ (red) and the vertical velocity variance (blue). The dashed black box denotes the eclipse period, and the solid vertical lines depict the period of totality
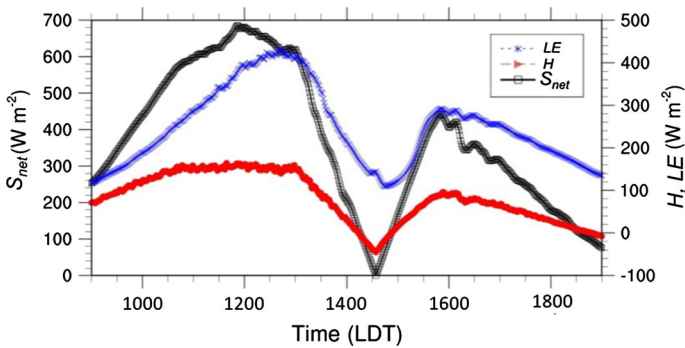

Fig. 10 Net shortwave radiative flux (black), sensible heat flux (red), and latent heat flux (blue) from the simulation

compared to the observations, allowing evaluation of model performance under these unique conditions.

The observations were generally consistent with other studies of partial and total solar eclipses. The primary findings show that, as the incoming shortwave radiative flux decreases to zero, surface and 1.5-m air temperatures also decrease. A time lag in the minimum in surface temperature of ≈ 4 min is consistent with that of 7 min found by Eaton et al. (1997). The 1.5-m a.g.l. temperature had a time lag of 13 min and is consistent with the range of values reported in the literature (e.g., Anderson 1999). The time lag is generally longer for temperature at levels further from the ground, as it takes longer for surface-based conduction/convection
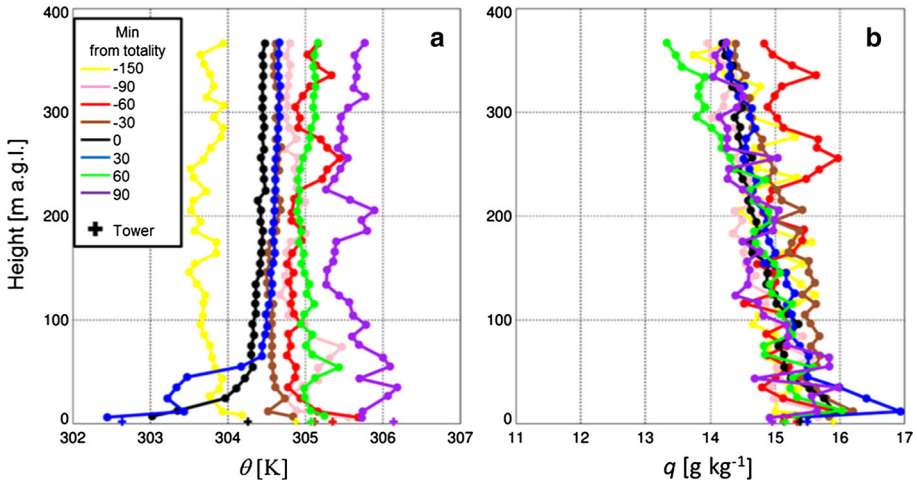
Fig. 11 Vertical profiles of potential temperature (left) and specific humidity (right) obtained from the sUAS platform during eight separate flights prior to, after, and during the eclipse. Each colour is an individual flight as noted in the legend. Data averaged into 10-m bins. Mean tripod measurements during each flight are shown by a "+"
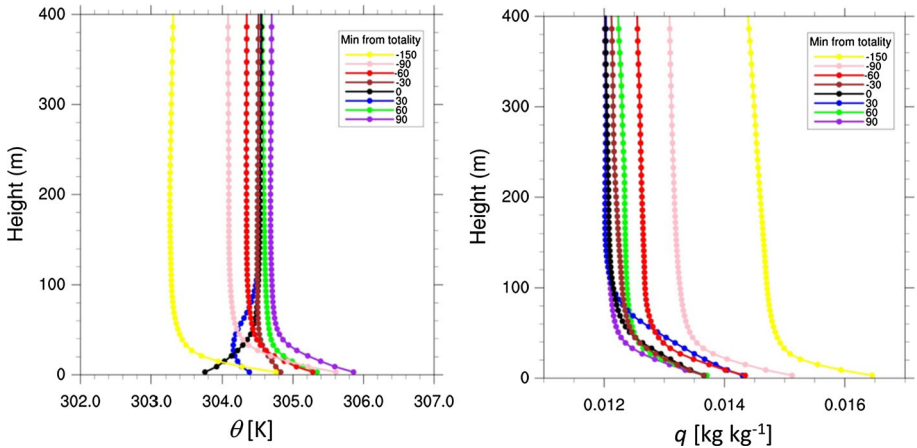
Fig. 12 Vertical profiles of potential temperature (left) and water vapour mixing ratio (right) from the simulation during eight separate flights prior to, after, and during the eclipse. Each colour is an individual flight as noted in the legend

to affect these levels. However, the time lag is also dependent on the local atmospheric and surface conditions, such as terrain and vegetation. Values of surface sensible heat flux also decreased to zero, consistent with Eaton et al. (1997), Foken et al. (2001), Mauder et al. (2007), and Turner et al. (2018). Also, TKE decreased substantially, as forcing for vertical motion diminished, which was consistent with Krishnan et al. (2004). Vertical profiles of TKE from the LES model also showed decreases throughout the ABL until just after totality before increasing as the eclipse ended (Fig. 13). These decreases are maximized near the middle of the ABL and are less near the ABL top; the results are consistent with those found in simulations of the onset of the nocturnal inversion (e.g., Moeng and Sullivan 1994; Mironov

Fig. 13 Vertical profile of turbulent kinetic energy $\bar{e}$. Colours represent times as in Fig. 12
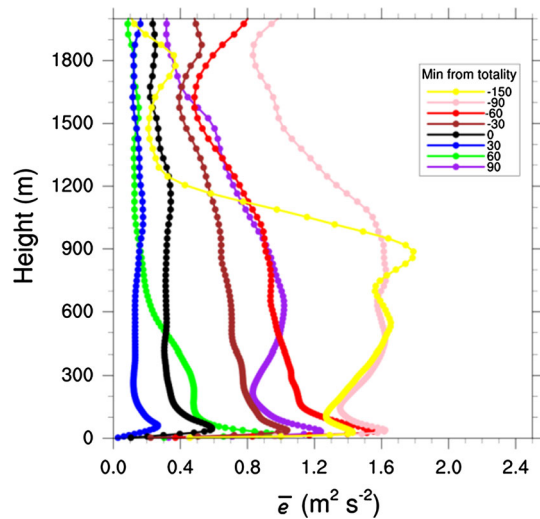
and Sullivan 2016). It is interesting to note that by 60 min after eclipse totality low-level TKE is increasing, and is still decreasing at a height of ≈ 1000 m a.g.l. By 90 min after eclipse totality, TKE is increasing throughout the ABL. This vertical time lag is consistent with TKE being driven by surface heating. It is also notable that there were numerous cumuli atop the ABL prior to the eclipse, which dissipated and led to clear skies during totality; cumuli then redeveloped as the eclipse ended as was observed (not shown). This ABL evolution was reproduced in the simulation (Fig. 5). Also notable was the rapid increase in near-surface dewpoint that occurred just prior to totality, peaking just after totality then decreasing soon after to near pre-eclipse levels. The post-eclipse increase in low-level moisture that was seen at this site and other sites within the path of totality and reproduced in the simulation merits further study.

Whereas surface meteorological and flux measurements have been reported during previous total eclipses, vertical profiles through the lower atmosphere have been largely unattainable due to limitations in instrumentation with the exception of Turner et al. (2018). With the use of the sUAS platform, we have obtained vertical profiles of temperature and moisture before, during, and after the eclipse to provide insight into ABL dynamics during this period. We found substantial cooling in the near surface (≈ 50 m) as the eclipse approached totality, which was followed by recovery as the partial eclipse ended. Above this height, only modest changes were observed, with the time scale of the eclipse having a smaller influence on deeper ABL turbulence around totality. Our observations are consistent with Turner et al. (2018) who observed the partial eclipse at the Atmospheric Radiation Measurement (ARM) site in northern Oklahoma, USA.

The LES model generally reproduced the observations well, in terms of timing and magnitude of changes in temperature, moisture and sensible and latent heat fluxes, although with a few caveats. The model tended to slightly underestimate the diurnal range and decrease in temperature during the eclipse and tended to overestimate the sensible heat flux compared to the point observations. One limitation is that the simulation was for a homogeneous surface and the results shown are domain averages. Also, the model had a dry bias both near the surface and aloft. Some of these differences might be attributed to using a sounding for initialization that was synoptically representative but was not representative of the local terrain

surrounding the Ten Mile area. More importantly, these results, combined with other high-resolution numerical models (e.g., the High-Resolution Rapid Refresh) should be further examined to highlight weaknesses in model parametrizations so that improvements can be made.

References

Anderson J (1999) Meteorological changes during a solar eclipse. Weather 54:207–215

Anderson RC, Keefer DR (1975) Observations of the temperature and pressure changes during the 30 June 1973 solar eclipse. J Atmos Sci 32:228–231

Anderson RC, Keefer DR, Myers OE (1972) Atmospheric pressure and temperature changes during the 7 March 1970 Solar eclipse. J Atmos Sci 29:583–587

Buban MS, Ziegler CL, Mansell ER, Richardson YP (2012) Simulation of dryline misovortex dynamics and cumulus formation. Mon Weather Rev 140:3525–3551

Coniglio MC, Stensrud DJ, Wicker LJ (2006) Effects of upper-level shear on the structure and maintenance of strong quasi-linear mesoscale convective systems. J Atmos Sci 63:1231–1252

Deardorff JW (1978) Efficient prediction of ground surface temperature and moisture, with inclusion of a layer of vegetation. J Geophys Res 83:1889–1903

Dumas EJ., Lee TR, Buban MS, Baker CB (2016) Small unmanned aircraft system (sUAS) measurements during the 2016 verifications of the origins of rotation in tornadoes experiment southeast (VORTEX-SE). NOAA technical memorandum OAR ARL-273. https://doi.org/10.7289/v5/tm-oar-arl-273

Eaton FD, Hines JR, Hatch WH, Cionco RM, Byers J, Garvey D, Miller DR (1997) Solar eclipse effects observed in the planetary boundary layer over a desert. Boundary-Layer Meteorol 83:331–346

Foken TB, Wichura Klemm O, Gerchau J, Winterhalter M, Weidinger T (2001) Micrometeorological measurements during the total solar eclipse of August 11, 1999. Meteorol Z 10:171–178

Founda DD, Melas Lykoudis S, Lisardis I, Gerasopoulos E, Kouvarakis G, Petrakis M, Zerefos C (2007) The effect of the total solar eclipse of 29 March 2006 on meteorological variables in Greece. Atmos Chem Phys 7:5543–5553

Krishnan PP, Kunhikrishnan K, Muraleedharan S, Nair Ravindran S, Ramachandran R, Subrahamanyam DB, Venkata Ramana M (2004) Observations of the atmospheric surface layer parameters over a semi arid region during the solar eclipse of August 11th 1999. Proc Indian Acad Sci 113:353–363

Lee TR, Buban MS, Dumas E, Baker CB (2017) A new technique to estimate sensible heat fluxes around micrometeorological towers using small unmanned aircraft systems. J Atmos Ocean Technol 34:2103–2112

Lee TR, Buban M, Palecki MA, Leeper RD, Diamond HJ, Dumas E, Meyers TP, Baker CB (2018) Great American Eclipse data may fine-tune weather forecasts. Eos 99(11):19–22

Lee TR, Buban MS, Dumas E, Bruce Baker C (2019) On the use of rotary-wing aircraft to sample near-surface thermodynamic fields: results from recent field experiments. Sensors 19(1):10. https://doi.org/10.3390/s19010010

Mauder M, Desjardins RL, Oncley S, MacPherson I (2007) Atmospheric response to a partial solar eclipse over a cotton field in central California. J Appl Meteorol Climatol Soc 46:1792–1803

Mironov D, Sullivan PP (2016) Second moment budgets and mixing intensity in the stably stratified atmospheric boundary layer over thermally heterogeneous surfaces. J Atmos Sci 73:449–464

Moeng CH, Sullivan PP (1994) A comparison of shear-and buoyance-driven planetary boundary layer flows. J Atmos Sci 51:999–1022

Peckham SE, Wilhelmson RB, Wicker LJ, Ziegler CL (2004) Numerical simulation of the interaction between the dryline and horizontal convective rolls. Mon Weather Rev 132:1792–1812

Segal M, Turner RW, Prusa J, Bitzer RJ, Finley SV (1996) Solar eclipse effect on shelter air temperature. Bull Am Meteorol Soc 77:89–99

Stewert RB, Rouse WR (1974) Radiation and energy budgets at an arctic site during the solar eclipse of July 10, 1972. Arct Alp Res 6:231–236

Subrahamanyam DB, Anurose TJ, Mohan M, Santosh M, Kiran Kumar NVP, Sijikumar S, Prijith SS, Aloystus M (2011) Atmospheric surface-layer response to the annular solar eclipse of 15 January 2010 over Thiruvananthapuram, India. Boundary-Layer Meteorol 141:325–332

Turner DD, Wulfmeyer V, Behrendt A, Bonin TA, Choukulkar A, Newsom RK, Cook DR (2018) Response of the land-atmosphere system over north-central Oklahoma during the 2017 eclipse. Geophys Res Lett 45:1668–1675

Wicker LJ, Skamarock W (2002) Time-splitting methods for elastic models using forward time schemes. Mon Weather Rev 130:2088–2097

Wicker LJ, Wilhelmson RB (1995) Simulation and analysis of tornado development and decay within a three-dimensional supercell thunderstorm. J Atmos Sci 52:2675–2703